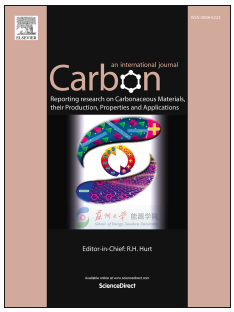

Topological defect and sp^3/sp^2 carbon interface derived from ZIF-8 with linker vacancies for oxygen reduction reaction

Haixing Gao, Shuo Wang, Weng-Chon (Max) Cheong, Kaixi Wang, Huifang Xu, Aijian Huang, Junguo Ma, Jiazhan Li, Weng-Fai (Andy) Ip, Kwan San Hui, Duc Anh Dinh, Xi Fan, Feng Bin, Fuming Chen, Kwun Nam Hui

PII: S0008-6223(22)00851-X

DOI: https://doi.org/10.1016/j.carbon.2022.10.030

Reference: CARBON 17600

To appear in: *Carbon*

Received Date: 22 June 2022

Revised Date: 9 October 2022

Accepted Date: 14 October 2022

Please cite this article as: H. Gao, S. Wang, W.-C.(M.) Cheong, K. Wang, H. Xu, A. Huang, J. Ma, J. Li, W.-F.(A.) Ip, K. San Hui, D.A. Dinh, X. Fan, F. Bin, F. Chen, K.N. Hui, Topological defect and sp^3/sp^2 carbon interface derived from ZIF-8 with linker vacancies for oxygen reduction reaction, *Carbon* (2022), doi: https://doi.org/10.1016/j.carbon.2022.10.030.

CRediT authorship contribution statement

Haixing Gao: Conceptualization, Methodology, Investigation, Formal analysis, Investigation, Data curation, Drawing, Writing – original draft, Visualization. **Shuo Wang:** Methodology, Investigation, Formal analysis, Data curation, Drawing, Writing – original draft, Visualization. **Weng-Chon (Max) Cheong:** Conceptualization, Validation, Writing – review & editing, Visualization, Supervision, Funding acquisition. **Kaixi Wang:** Investigation. **Huifang Xu:** Investigation. **Aijian Huang**: Investigation, Formal analysis. **Junguo Ma**: Conceptualization, Writing – review & editing. **Jiazhan Li**: Funding acquisition, Formal analysis. **Weng-Fai (Andy) Ip:** Funding acquisition, Writing – review & editing. **Kwan San Hui:** Funding acquisition, Writing – review & editing. **Duc Anh Dinh:** Writing – review & editing. **Xi Fan:** Writing – review & editing. **Feng Bin:** Writing – review & editing. **Fuming Chen:** Writing – review & editing. **Kwun Nam Hui:** Resources, Writing – review & editing, Supervision, Project administration, Funding acquisition.

Topological defect (pentagon)

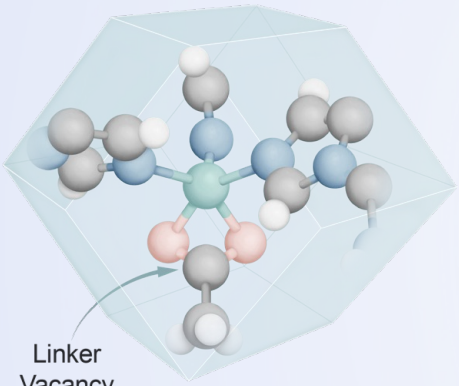

ZIF-8

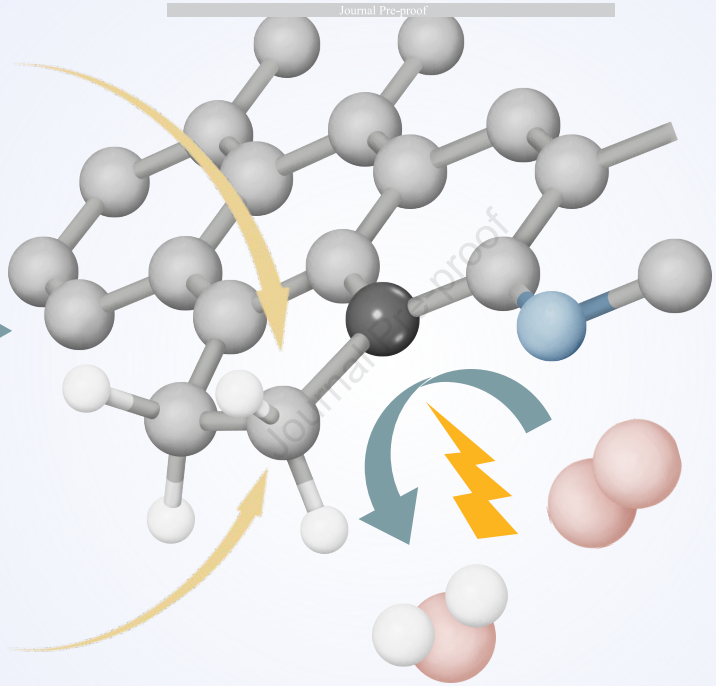

sp^3 hybridization carbon

Oxygen Reduction Reaction

E_{onset} = 1.05 V, $E_{1/2}$ = 0.873 V

in 0.1 M KOH

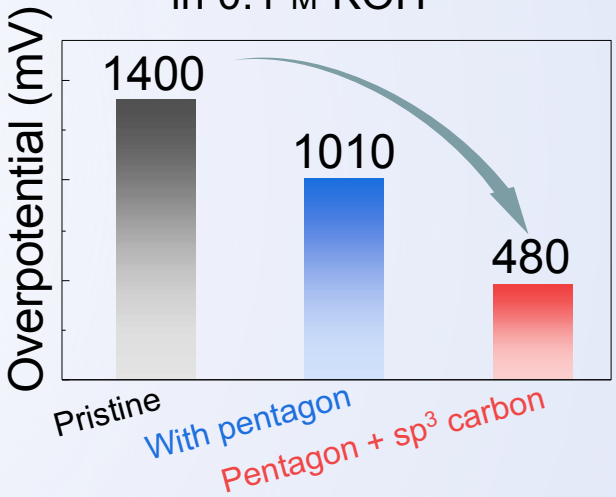

Topological Defect and sp^3/sp^2 Carbon Interface Derived from ZIF-8 with Linker Vacancies for Oxygen Reduction Reaction

Haixing Gao[a,#], *Shuo Wang*[a,#], *Weng-Chon (Max) Cheong*[b,#,*], *Kaixi Wang*[a], *Huifang Xu*,[a] *Aijian Huang*[c,d], *Junguo Ma*[d], *Jiazhan Li*[d], *Weng-Fai (Andy) Ip*,[b] *Kwan San Hui*[e,*], *Duc Anh Dinh*[f], *Xi Fan*[g], *Feng Bin*[h], *Fuming Chen*[i], *and Kwun Nam Hui*[a,*]

Haixing Gao, Shuo Wang, Kaixi Wang, Huifang Xu, Kwun Nam Hui

a. Joint Key Laboratory of the Ministry of Education, Institute of Applied Physics and Materials Engineering, University of Macau, Macao S.A.R. 999078, P. R. China

Weng-Chon (Max) Cheong, Weng-Fai (Andy) Ip

b. Department of Physics and Chemistry, Faculty of Science and Technology, University of Macau, Macao S.A.R. 999078, P. R. China

Aijian Huang

c. School of Electronics Science and Engineering, University of Electronic Science and Technology of China, Chengdu 610054, P. R. China

d. Department of Chemistry, Tsinghua University, Beijing 100084, P. R. China

Junguo Ma, Jiazhan Li

d. Department of Chemistry, Tsinghua University, Beijing 100084, P. R. China

Kwan San Hui

e. School of Engineering, Faculty of Science, University of East Anglia, Norwich, NR4 7TJ, United Kingdom

Duc Anh Dinh

f. NTT Hi-Tech Institute, Nguyen Tat Thanh University, Ho Chi Minh City 700000, Vietnam

Xi Fan

g. Ningbo Institute of Materials Technology, Engineering, Chinese Academy of Sciences, Ningbo, 315201, P. R. China

Feng Bin

h. State Key Laboratory of High-Temperature Gas Dynamics, Institute of Mechanics, Chinese Academy of Sciences, Beijing 100190, P. R. China

Fuming Chen

i. State Key Laboratory of Optic Information Physics and Technologies, School of Physics and Telecommunication Engineering, South China Normal University, Guangzhou, China 510006, P. R. China

# These authors contributed equally to this work and should be considered co-first authors.

* Corresponding author. E-mail: maxcheong@um.edu.mo (Weng-Chon (Max) Cheong). k.hui@uea.ac.uk (Kuan San Hui). bizhui@um.edu.mo (Kwun Nam Hui).

Keywords: metal-free, carbon-based materials, metal–organic framework, defect chemistry, metal–air battery

Defects in nanocarbon materials can trigger their intriguing electrochemical properties and potential applications, but their synthesis is challenging. Herein, we report the synthesis of ultrathin nitrogen-doped carbon nanosheets with intrinsic defects through the pyrolysis of ZIF-8 with linker vacancies. The as-synthesized electrocatalyst exhibits excellent oxygen reduction reaction (ORR) activity with an onset potential and half-wave potential of 1.05 and 0.873 V vs. RHE, respectively, outperforming the reported metal-free ORR electrocatalysts. It also shows a commercial Pt/C-comparable performance in zinc–air battery with a power density of 154.4 mW cm^{-2}. Characterization and DFT calculation results suggest the adjacent sp^3-carbon in carbon pentagon can significantly strengthen the adsorption and activation of oxygen molecules on sp^2-carbon, hence the potential determining step is altered and ORR overpotential is lowered. This work highlights a promising green synthesis strategy of MOF-derived metal-free nanocarbon materials for wide application in advanced energy technologies.

1. Introduction

The synthesis and application of nanocarbon materials (NCMs) is a highly active topic in chemistry and materials science.[1,2] Since carbon atoms have varied bonding forms, different kinds of defects (edges, vacancies, holes, heteroatom doping, topological defects, and hybridization states) may exist in NCMs, evolving their intriguing chemical properties.[3,4] Therefore, the regulation of defects on NCMs is critical to energy storage and conversion applications such as batteries, supercapacitors, and catalysis.[5-8]

Heteroatom doping is a widely adopted strategy to tune the catalytic properties of NCMs.[9] Nitrogen, sulfur, phosphorus, boron, and other dopants are believed to change the electronic structure of adjacent carbon atoms or cause geometrical distortions.[10,11] Thereby, the adsorption of catalytic reaction intermediates is optimized, and the performance is improved. However, heteroatom doping often leads to complex catalyst structures, and the active sites for catalytic reactions in these catalysts remain controversial.[12]

In recent years, the role of the intrinsic defects (topological defects, hybridization states) in NCMs on the catalytic process has to be concerned. Yao revealed the oxygen reduction reaction (ORR) activity of graphene with 585 defect, which exhibits superior performance to nitrogen-doped carbon.[13] Hu also demonstrated the potential carbon pentagon and zigzag edges in NCMs with excellent ORR performance.[14] Wei systematically studied the effects of topological defects and nitrogen doping species on ORR performance and found that the adjacent carbon pentagon and heptagon at the edge can bring extremely low ORR overpotential.[15] Meanwhile, Yao directly observed topological defects tend to form at the edge of NCMs, which leads to excellent electrochemical performance.[16] Although the above studies have proposed the structural models of a variety of potential active sites, the density of the generated intrinsic carbon defects is usually very low according to the second law of thermodynamics, and the limited active sites hamper the catalytic activity and application performance. Controllable and large-scale synthesis of high-performance defect-rich NCMs is challenging.

Various synthetic strategies have been reported successively to introduce a large number of carbon defects recently. Mu derived carbon pentagon-defect-rich NCMs from in situ alkali etching of fullerene.[17] Ma obtained three-dimensional nitrogen-doped porous carbon with rich sp^3/sp^2 carbon interfaces by radical polymerization and pyrolysis of ionic liquids.[18] Chen reported a volatile salt etching strategy to obtain NCMs with abundant sp^3 hybridized carbon atoms through pyrolysis.[19] However, these methods result in high production costs or low

yields due to expensive precursors or difficult-to-control processes. It is imperative to develop synthetic methods that can effectively control various defects.

Herein, we introduce the synthesis of ultrathin metal-free nitrogen-doped carbon nanosheets with rich carbon defects (D-NCNS) via the pyrolysis of ZIF-8 with linker vacancies (ZIF-8-LV). Characterizations reveal that D-NCNS possesses abundant edge, carbon pentagon, and sp^3-carbon atoms. Owing to the abundant defects and improved mass/electron transfer efficiency, the obtained electrocatalyst exhibits excellent ORR activity with an onset potential (E_{onset}) and half-wave potential ($E_{1/2}$) of 1.05 V and 0.873 V vs. RHE, respectively, outperforming the commercial Pt/C and reported NCMs. Meanwhile, the D-NCNS exhibits a Pt/C-comparable performance as a cathode catalyst in Zn–air batteries (ZABs). Density functional theory (DFT) calculation results suggest the adjacent sp^3-carbon in carbon pentagon can strengthen the adsorption and activation of oxygen molecules on sp^2-carbon significantly. The potential determining step is altered, the overpotential is lowered, and the ORR performance is improved. Interestingly, the calculation results imply that nitrogen doping has no positive effect on ORR performance. This work provides a facile, cheap, and large-scale synthesis strategy to obtain abundant active defect sites for high-performance electrochemical applications.

2. Experimental Section

2.1 Materials

Zinc acetate ($Zn(CH_3COO)_2 \cdot 2H_2O$) and 2-methylimidazole were purchased from Macklin Chemical Co., Ltd. Boric acid (H_3BO_3) was supplied by Aladdin Chemical Co., Ltd. NaCl, KOH, ethanol, and isopropanol were purchased from Sinopharm Chemical Reagent Co., Ltd. All chemicals were used directly if without additional notification. Deionized (DI) water was produced by Millipore Milli-Q Integral 10 Water Purification System.

2.2 Synthesis of precursors and electrocatalysts

Synthesis of ZIF-8-LV: $Zn(CH_3COO)_2 \cdot 2H_2O$ (5 mmol) mixed with H_3BO_3 (5 mmol) were dissolved in deionized water (30 mL), 2-methylimidazole (80 mmol) was dissolved in another deionized water (30 mL). The two solutions were mixed and stirring 1 h at room temperature. Then, the solution was transferred to a Teflon-lined stainless steel autoclave (100 mL) and heated to 175 °C for 3 h. After cooling to room temperature, the ZIF-8-LV was collected, washed with deionized water, and dried at 60 °C under a vacuum overnight. For comparison, ZIF-8 without added H_3BO_3 was also synthesized.

Synthesis of D-NCNS: ZIF-8-LV powder (0.1 g) and NaCl (1.0 g) were physically mixed by grinding, then the mixture was placed in a graphite crucible, and transferred into a tube furnace, heated to 1000 °C at 5 °C min^{-1} and kept for 3 h under flowing N_2. After being washed with plenty of deionized water and dried under vacuum overnight, the obtained product is denoted as D-NCNS. To investigate the effect of NaCl, the different mass ratios between ZIF-8 and NaCl were mixed. NC, NCNS, D-NC, D-NCNS (1/1), D-NCNS (10/1) (D-NCNS, the ratio of 10/1 if not indicated later), and D-NCNS (50/1) were obtained by calcining pure ZIF-8, ZIF-8 + NaCl (m_{NaCl} : m_{ZIF-8} = 10 : 1), pure ZIF-8-LV, ZIF-8-LV + NaCl (m_{NaCl} : $m_{ZIF-8-LV}$ = 1 : 1), ZIF-8-LV + NaCl (m_{NaCl} : $m_{ZIF-8-LV}$ = 10 : 1), and ZIF-8-LV + NaCl (m_{NaCl} : $m_{ZIF-8-LV}$ = 50 : 1), respectively.

2.3 Physical characterization

The morphology of the electrocatalysts was portrayed by scanning electron microscopy (SEM, Zeiss Sigma) and transmission electron microscopy (TEM, Talos F200X, FEI, accelerating voltage of 200 kV). The crystallographic structure was determined using an Ultima IV X-ray diffractometer (XRD, Rigaku) equipped with Cu Kα radiation (λ = 1.5418 Å), and the data were collected in the Bragg–Brentano mode with a scan rate of 10° min^{-1}. X-ray photoelectron spectroscopy (XPS) was offered out on an ESCALAB Xi+ XPS Microprobe (Thermo Scientific). Al Kα (photon energy 1,486.7 eV) was used as the excitation source for XPS. The Raman spectroscopy was performed on LABHRev-UV (Horiba) operated at 633 nm of wavelength. Nitrogen isotherm adsorption/desorption curve was collected on 3Flex Adsorption Analyzer (Micromeritics). The specific surface area is calculated based on the Brunauer–Emmett–Teller model.

2.4 Electrochemical measurements

The electrochemical tests were performed under a three-electrode system using an electrochemical workstation (VMP-300 bio-logic system). A graphite rod and Ag/AgCl (saturated KCl) electrode served as the counter electrode and the reference electrode, respectively. All measured potentials were calibrated to the reversible hydrogen electrode (RHE) according to the equation:

$$E_{RHE} = E_{Ag/AgCl} + 0.0591 \times pH + 0.197\ V$$

A rotating disk electrode (RDE, 5 mm diameter) was the working electrode. Electrocatalyst (10.0 mg) was dispersed in a mixture composed of H_2O (743 μL), isopropanol (247 μL), and 5 wt% Nafion solution (10 μL) and subsequently under ultrasonic for 2 h. The resulting ink (10

μL) was loaded on the working electrode, achieving a catalyst loading of 0.5 mg cm^{-2}, followed by evaporation of the solvent in air. The loading of commercial 20% Pt/C catalyst is 0.2 mg cm^{-2} was used as the ORR benchmark. The ORR test was performed in 0.1 M KOH with saturated oxygen. The linear sweep voltammetry (LSV) curve was recorded at a scan rate of 5 mV s^{-1} at 1600 rpm.

The kinetic current density (J_k) was calculated by the Koutecky-Levich equation:

$$1/J = 1/J_L + 1/J_k$$

where J, J_k, and J_L are the measured, kinetic, and limiting current density, respectively.

According to the Tafel equation, use the LSV profile data to calculate the Tafel slope:

$$\eta = b \log (j_k / j_0)$$

where η is the overpotential calculated by $\eta = |1.23\ V - E_{RHE}|$, j_k is the kinetic current density, j_0 is the exchange current density, and b is the Tafel slope.

Electrochemical impedance spectroscopy (EIS) analysis was carried out with a superimposed 10 mV sinusoidal voltage in the frequency range of 10 kHz to 0.1 Hz at 8 points per decade. All data were recorded in a single sine mode. The impedance spectra were fitted using Z-fit method with "EC-Lab" software.

Electrochemical surface area (ECSA) was evaluated by the double-layer capacitance (C_{dl}) of the electrocatalysts. C_{dl} was measured by CV at different scan rates in the non-Faradaic potential range. The value of C_{dl} was half of the slope derived from the difference between anode and cathode current density ($\Delta j = j_a - j_c$) against the scan rate. The C_{dl} is converted into the ECSA using the specific capacitance value for a flat standard electrode with 1 cm^2 of real surface area (C_s), the C_s is generally in the range of 20 to 60 μF cm^{-2}. Here we use the average value of 40 μF cm^{-2} per cm_{ECSA}^2 to calculate the ECSA.[20]

$$ECSA = C_{dl}/C_s$$

The normalized specific J_k ($J_{k\ ECSA}$) can be obtained by:

$$J_{k\ ECSA} = J_k/ECSA$$

For RRDE measurement, the electron transfer number (n) and peroxide intermediate production percentage (H_2O_2%) were calculated according to the following formula:

$$n = 4 \times I_d/(I_d + I_r/N)$$

$$H_2O_2\% = 200 \times (I_r/N)/(I_d + I_r/N)$$

where I_d is the disk current, I_r is the ring current, and N is the current collection efficiency at the ring, which was 0.37.

The stability was assessed by current-time chronoamperometric measurements at 0.8 V vs. RHE. The stability was also measured by LSV curves before and after 12000 CV cycles across the potential window of 0.6 to 1.0 V vs. RHE in an O_2-saturated 0.1 M KOH solution.

2.5 Zn–air battery assembles

To make a Zn–air battery, 10.0 mg electrocatalyst was mixed with 980 μL ethanol + 20 μL 5 wt% Nafion solution and subsequently under ultrasonic for approximately 2 h. The resulting ink (113 μL) was loaded on carbon cloth, achieving a catalyst loading of 1.0 mg cm^{-2}, followed by evaporation of the solvent in the air, and then used as an air cathode. A zinc plate is used as the anode. KOH electrolyte solution (6.0 M) was used as electrolyte. Use two electrodes to test the homemade Zn–air battery at room temperature.

2.6 Theoretical Calculations

Spin–polarized density functional theory (DFT)[21] is conducted in the Vienna ab initio simulation package (VASP 6.2.0).[22] We adopt the projected augmented–wave method (PAW)[23] potentials, and the exchange–correlation energy of the general gradient approximation (GGA) in the scheme proposed by Perdew–Burke–Ernzerh (PBE).[24] The cut–off kinetic energies for the plane waves are set to 450 eV for all the calculations. The convergence tolerance of energy and force on each atom during structure relaxation are less than 10^{-5} eV and 0.02 eV $Å^{-1}$. A set of Monkhorst–Pack mesh K points of 2 × 2 × 1 and 4 × 4 × 1 are used to sample the Brillouin zone for geometry optimization and electronic structural calculations.[25] The *c* axis is set to 15 Å to ensure sufficient vacuum to avoid interactions between two periods. Grimme's DFT–D3 scheme was used to describe the van der Waals (vdW) interactions in the systems.[26,27]

For ORR process, the oxygen will first adsorb on the active site and then each step obtains an electron and generates OH- while forming *O, *OH and *OOH intermediates respectively. The thorough four-electron pathway in the alkaline medium is as follows:

$$O_2 + 2H_2O\ (l) + 4e^- \rightarrow *O_2 + 2H_2O\ (l) + 4e^- \quad (5)$$

$$*O_2 + 2H_2O\ (l) + 4e^- \rightarrow *OOH + OH^- + H_2O\ (l) + 3e^- \quad (6)$$

$$*OOH + OH^- + H_2O(l) + 3e^- \rightarrow *O + H_2O\ (l) + 2(OH^- + e^-) \quad (7)$$

$$*O + H_2O\ (l) + 2(OH^- + e^-) \rightarrow *OH + 3OH^- + e^- \quad (8)$$

$$*OH + 3OH^- + e^- \rightarrow 4OH^- \quad (9)$$

Here, "l" denotes the liquid state and "*" denotes the adsorbed species on the active site. The OER process is the opposite.

3. Results and Discussion

3.1 Synthesis and characterization of ZIF-8-LV

The synthesis of D-NCNS is schematically described in **Figure 1**. First, ZIF-8-LV was synthesized by a hydrothermal method with zinc acetate, 2-methylimidazole, and boric acid. For comparison, the ZIF-8 without the addition of boric acid was also synthesized.

The crystal structure of ZIF-8 with different synthesis conditions was detected by X-ray powder diffraction (XRD, Figure S1 in Supplementary Material), showing that the ZIF-8 precursors were successfully synthesized, and the addition of H_3BO_3 did not affect the crystal phase of ZIF-8. It is noteworthy that the diffraction peaks of both ZIF-8 and ZIF-8-LV show negative shift compared with the ZIF-8 simulated pattern. Further analysis of the diffraction peak of (110) facet exhibited a tensile strain of 1.65% and 1.88% in ZIF-8 and ZIF-8-LV, respectively (Table S1). The lattice strain may be caused by the defect in the as-synthesized ZIF-8. [28]

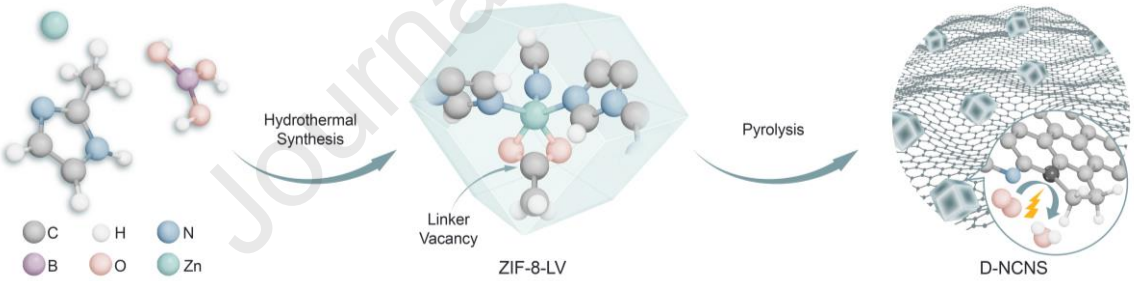

Figure 1. Scheme of the synthesis route to D-NCNS electrocatalysts.

X-ray photoelectron spectroscopy (XPS) was adopted to investigate the content and chemical states of the elements in ZIF-8 and ZIF-8-LV (**Figures 2b–d**, **S2, and S3**). The ZIF-8 and ZIF-8-LV is mainly composed of carbon, nitrogen, oxygen, and zinc. The element content of the precursor measured by XPS is listed in **Table S2**. It is noteworthy that no boron element was found in the formed ZIF-8-LV (Figure S3e).[29] The complete removal of boric acid during the post-synthesis treatment is possibly due to its great solubility in water, and the ability to escape through the pore of ZIF-8. In the ideal ZIF-8 crystal, each Zn is bonded to four 2-methylimidazole ligands. Interestingly, the N/Zn ratio of ZIF-8-LV through a hydrothermal transformation process with the addition of H_3BO_3 was 2.51, which was significantly lower

than the ZIF-8 synthesized without H_3BO_3 (3.61). In Figure 2b, three type nitrogen were found in both samples, namely the imidazole groups (N_imidazole), the presence of secondary amines (-NH-), and Zn-N.[30] Meanwhile, the Zn^{2+} cations in the ZIF-8-LV coordinate with CH_3COO^- anions can be confirmed by the increased CH_3COO-Zn peak area from XPS (Figure 2c). Moreover, the coordination of CH_3COO^- anions leads to the increase of area ration of Zn-CH_3COO in Zn 2p peaks (Figure 2d). These phenomena indicate the partial substitution of 2-methylimidazole by acetate anions in ZIF-8 and ZIF-8-LV, where the substitution in the latter is higher.

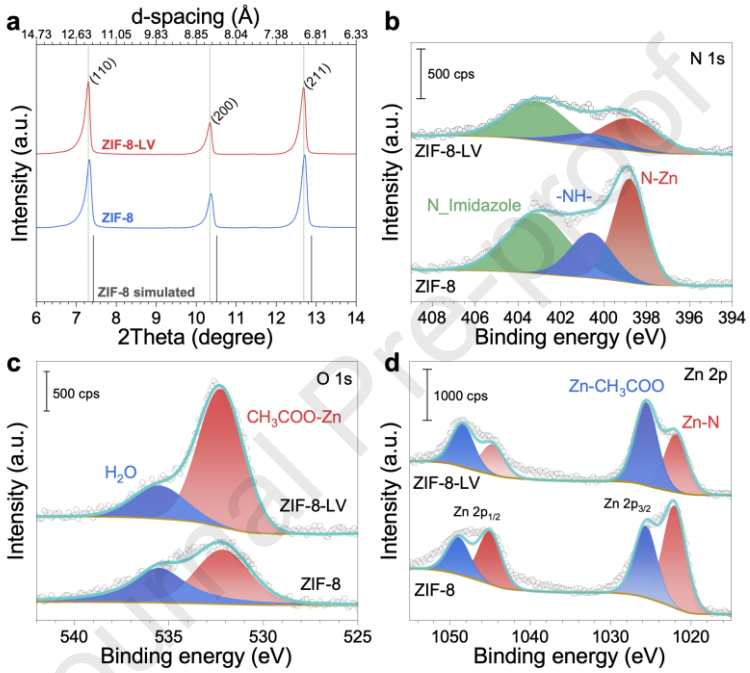

Figure 2. Structural characterization of ZIF-8-LV and ZIF-8. (a) Experimental and simulated diffraction patterns. (b–d) High-resolution XPS spectrum of N 1s (b), O 1s (c), and Zn 2p (d).

Different from other MOFs, typical zeolitic imidazolate frameworks (ZIFs) exhibit unusual chemical and thermal stability in an aqueous and alkaline solution.[29] Previously, Zhang and co-workers have studied the influence of water and acid gas on the formation of vacancies in ZIF-8 through theoretical computation.[30] In our synthesis procedure, H_3BO_3 undergoes stronger ionization in hydrothermal conditions, resulting in an overall stronger weak acidity of the solution, which affects the coordination and precipitation equilibrium between Zn^{2+} cations and 2-methylimidazole. With a weakened coordination between Zn^{2+} cations and 2-methylimidazole, a higher amount of acetate anions coordinate with Zn^{2+} cations, leading to the deficiency of 2-methylimidazole in the resultant ZIF-8-LV. This deficiency in the precursor is inherited by the product, facilitating the construction of a defect-rich product.

3.2 Synthesis and characterization of D-NCNS

After the synthesis of the precursor, it is mixed and ground uniformly with a certain amount of NaCl. Subsequently, the mixture is transferred to a tube furnace for calcination under the protection of nitrogen gas. Finally, the samples were obtained after the removal of NaCl by thoroughly washing with water. The NaCl plays several roles in the pyrolysis [31,32]: (i) The molten NaCl acts as a template for the formation of carbon nanosheets. (ii) The Na^+ cations can intercalate into the lamellar carbon nanosheets, leading to a decreased thickness. (iii) The molten NaCl can trap and dissolve the carbon intermediates generated during the ZIF-8 pyrolysis, leading to an increased yield of the nanocarbon materials. (iv) The Cl^- anions can combine with the Zn atoms in the ZIF-8 to form volatile $ZnCl_2$, which is a poregen that can increase the specific surface area of the nanocarbon materials.

XRD patterns (**Figures S4** and **S5**) show that zinc volatilized at a high temperature of 1000 °C as no peaks of zinc and related compounds were found. At the same time, no NaCl peak was found, indicating that the washing process has removed NaCl. Two evident broad peaks, located at ~25° and ~43°, correspond to the (002) and (101) planes of graphitic carbon (JCPDS No. 41-1487), respectively.

As shown in **Figure 3a**, **Figure S6** and **Table S3**, compared with NC and D-NC, the N_2 adsorption/desorption isotherms of D-NCNS show evident hysteresis loops, indicating the presence of NaCl during calcination has caused the formation of mesoporous structure. The BET surface area of D-NCNS reaches 1707 $m^2 g^{-1}$, which is higher than NC (1282 $m^2 g^{-1}$) and D-NC (1339 $m^2 g^{-1}$). Meanwhile, the average pore size of D-NCNS (3.71 nm) is also larger than NC (2.64 nm) and D-NC (2.64 nm). The enlarged pore size and more exposed edge sites are is conducive to the efficient mass transfer process during the electrochemical reaction, thereby facilitating the catalytic efficiency.[33-35]

The resulting catalyst was tested using Raman spectroscopy to study the changes in the carbon structure. As shown in **Figure 3b** and **S7**, the Raman spectra of all catalysts can be divided into four peaks — G (~1587 cm^{-1}), D1 (~1330 cm^{-1}), D2 (~1200 cm^{-1}), and D3 (~1500 cm^{-1}). The G and D1 peaks correspond to the E_{2g}-symmetry in ideal graphitic lattice and A_{1g}-symmetry of disordered graphitic lattice, respectively, and the ratio of these peaks can be used to characterize the overall degree of graphitization of the carbon material.[36-38] In addition, D2 and D3 peaks are associated with carbon atoms outside the perfect graphene layer and with pentagon or heteroatoms within the graphene layer structure, respectively. The D1/G area ratio (A_{D1}/A_G) of the D-NC (2.46) is higher than NC (2.33) because the vacancies in the precursor are inherited by the calcination product. With the addition of NaCl, D-NCNS has a much higher

D1/G area ratio (2.61), indicating an increase in the overall degree of disorder.[39] An increase in the D3 peak area ratio can also be noted (**Table S4**), demonstrating the presence of more carbon pentagon structures or a higher proportion of nitrogen doping in D-NCNS than NC.[40] The obtained products were further investigated by XPS. The C 1s, N 1s, and O 1s peaks can be identified from the full survey XPS spectrum of the electrocatalyst (**Figures S8**–**S13**). Boron is undetectable in all catalysts. The content of the elements is summarized in **Table S5**. Compared with the nitrogen content of NC (4.29 at%), the D-NC shows a lower nitrogen content (3.78 at%) due to the absence of nitrogen-containing ligands in the precursors. However, with the addition of NaCl, the nitrogen content of D-NCNS is increased compared with D-NC, indicating that the molten NaCl contributes to the retention of N species during pyrolysis.[41] This condition is also evidenced by the comparison between the N content of NCNS (5.93 at%) and NC (4.29 at%). The nitrogen doping content of D-NCNS and NC is the same so the increase in the proportion of D3 peaks is likely to stem more from defects in the carbon, such as the carbon pentagon. In **Figure 3c**, the high-resolution C 1s spectrum can be deconvoluted into C sp^2, C sp^3, C-N, O-C-O, C=O, and π–π*, the peak position and area-based peak proportions in the XPS C 1s spectra of as-prepared materials are listed in **Table S6**. Notably, the C sp^3/sp^2 peak area ratio of NC and D-NCNS is 0.58 and 1.17, respectively. As summarized in **Figure 3d**, the proportion of D3 in the Raman spectrum increases substantially in D-NCNS compared with the original NC, whereas the XPS results also demonstrate the increase in sp^3 carbon defects in the carbon material, indicating that more carbon defects were introduced during the synthesis process.[18,19]

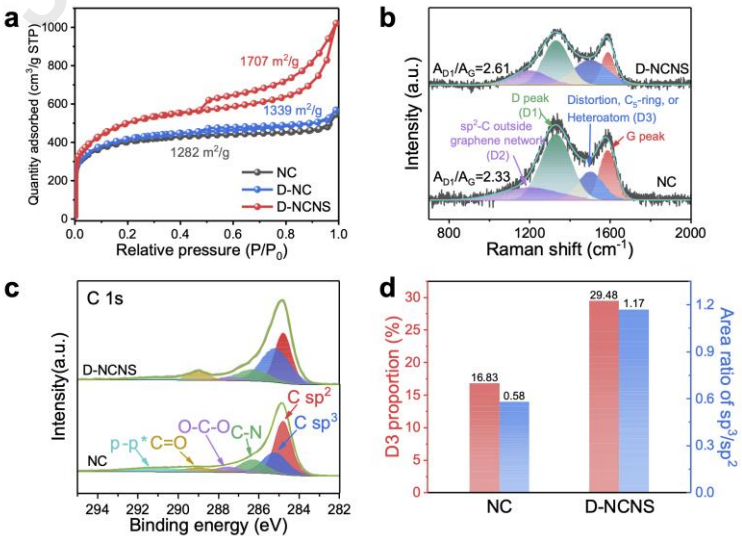

Figure 3. Structural characterization of NC, D-NC and D-NCNS. (a) N_2 adsorption/desorption isotherms, (b) Raman spectra, (c) high-resolution C 1s spectrum, (d) the corresponding proportion of D3 and the area ratio of sp^3/sp^2 of NC and D-NCNS.

Scanning electron microscopy (SEM) images (**Figures S14a** and **S15a**) present the well-dispersed polyhedral morphology of NC and D-NC derived from ZIF-8 with a size distribution ranging from 100 nm to 200 nm. However, the addition of H_3BO_3 did not have a significant effect on the morphology and no formation of by-products or amorphous compounds, as already confirmed by XRD.[42-44] After calcination, the precursor particles shrink isotopically and form solid dodecahedral NC and D-NC with a smooth surface. Interestingly, after mixing with an equivalent amount of NaCl, the ZIF-8-LV precursor anisotropically shrinks and the plane of the dodecahedron is partly collapsed while the edge stripes are maintained, forming a concave carbon nanopolyhedron structure, as shown in Figure S15b. With a further increase in the mass of NaCl to 10 times of ZIF-8-LV, the ZIF precursor volatilizes carbon-containing intermediates during the carbonization process, and these volatile intermediates are captured in the molten NaCl, forming ultrathin graphene-like flakes.[45,46] When the NaCl was removed by water, a unique architecture of nitrogen-doped carbon concave polyhedrons interface on ultrathin carbon nanosheets is formed, as shown in **Figure 4a**. Such a continuous structure facilitates the charge transfer process.[47]

The morphology and element distribution of D-NCNS was further evaluated using transmission electron microscopy (TEM) images. **Figure 4b** shows the shrinkage of the particles, forming a concave structure, which provides more accessible active sites in ORR. A magnified TEM image demonstrates that ZIF-8-derived concave carbon polyhedron with a rough surface is partly wrapped in and attached to carbon nanosheets (**Figure 4c**). Energy-dispersive X-ray spectroscopy (EDS) element mapping exhibited uniform distribution of C, N, and O in D-NCNS (**Figure S16**). The thickness of the carbon nanosheets are approximately 2.7–3.4 nm, corresponding to 8–10 graphene layers (**Figure 4d**). Based on the fast Fourier transform (FFT) analysis of the junction between the carbon polyhedra and nanosheets, we observed a relatively sharper ring from the nanosheets compared with that from the polydehra, indicating that the nanosheets possess higher graphitic crystallinity than the amorphous polyhedra.[19] The HRTEM results, combining the above-mentioned XPS and Raman spectroscopy analysis, imply a higher sp^2 content in carbon nanosheets and higher sp^3 content in carbon polyhedra; the sp^3/sp^2 carbon interfaces mainly gather at the carbon polyhedra–nanosheet homojunction. High-speed electron pathways can be facilitated by interfacial

interactions between carbon polyhedra and nanosheets, thereby accelerating the electron transfer process.[48]

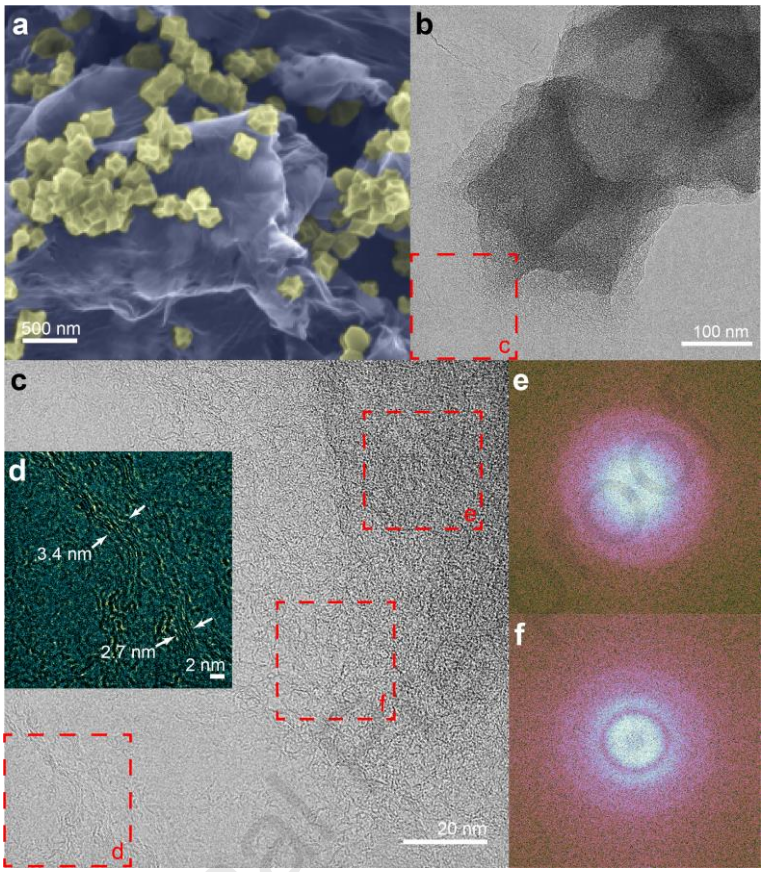

Figure 4. Morphology and crystallinity characterization of D-NCNS. (a) SEM image in false color. (b) TEM image. (c) HRTEM image. (d) Magnified area in false color. (e,f) FFT of the corresponding areas in (c).

3.3 ORR performance

The ORR performance of the as-obtained samples was examined in O_2-saturated 0.1 M KOH electrolyte. As shown in **Figure 5a**, the D-NCNS exhibits a 1.05 V vs. RHE of onset potential (E_{onset}, defined as the current density at –0.2 mA cm^{-2}), 0.873 V vs. RHE of half-wave potential ($E_{1/2}$), and 5.65 mA cm^{-2} of limited current density (J_L, defined at 0.20 V vs. RHE). These values are higher than the other synthesized catalysts and surpass the reported metal-free carbon-based catalysts (**Figure 5b** and **Table S7**).

The kinetic current density (J_k) is proportional to the intrinsic activity of the catalyst.[49,50] To characterize the intrinsic activity of the catalysts, the potential dependence of J_k for different catalysts is shown in **Figure S17**. Without H_3BO_3 and NaCl assistance, NC exhibits poor activity. The largest J_k of D-NCNS demonstrates the significantly enhanced ORR performance.

Meanwhile, the decreasing Tafel slopes confirm that the corresponding reaction kinetics becomes faster (**Figure 5c**). The electrochemical properties of the products obtained by calcination with different ratios of ZIF-8 and NaCl were tested to further investigate the effect of NaCl during calcination on the performance, as shown in **Figure S18**. The interface resistance of all catalysts is measured by electrochemical impedance spectroscopy (EIS), as shown in **Figure S19,** and the equivalent circuit elements are used to model the underlying oxygen reduction processes (**Figure S20**), the fit results is listed in the **Table S8.** The J_k of the electrocatalysts is further normalized by electrochemical surface area (ECSA, **Figure S21**) to eliminate the influence of the active area and obtain the intrinsic activity, as shown in **Figure 5d** and **S22**. After normalization, the D-NCNS catalyst still exhibited an enhanced current density compared with NC, D-NC, and NCNS. The normalized results suggest that the increased performance was not only due to an increase in specific surface area, but also the enhanced intrinsic activity of the active sites with the combination of carbon defect and interface.

The selectivity of catalysts in the oxygen reduction process is given in **Figure 5e**, the number of electron transfer (n) and the hydrogen peroxide yield (H_2O_2%) of D-NCNS is 3.90–3.96 and 1.88%–4.85% in the range of 0.20–0.80 V, which was close to Pt/C (3.91–3.96, 1.95%–4.12%), indicating that the reduction of O_2 is carried out a four-electron process on D-NCNS. The chronoamperometric response at 0.80 V vs. RHE of D-NCNS and Pt/C was measured to evaluate the stability of electrocatalysts (**Figure S23**). The current retention of D-NCNS is 82.4% after 40000 s, whereas that of Pt/C drops to 54% under the same condition. The LSV curve of D-NCNS and Pt/C before and after 12000 voltammetric cycles (**Figure 5f** and Figure S24) was also measured in O_2-saturated 0.1 M KOH at a rotating speed of 900 rpm. The Pt/C decreased 145 mV on $E_{1/2}$, while the D-NCNS electrocatalyst only decreased 18 mV, indicating good ORR durability of D-NCNS.

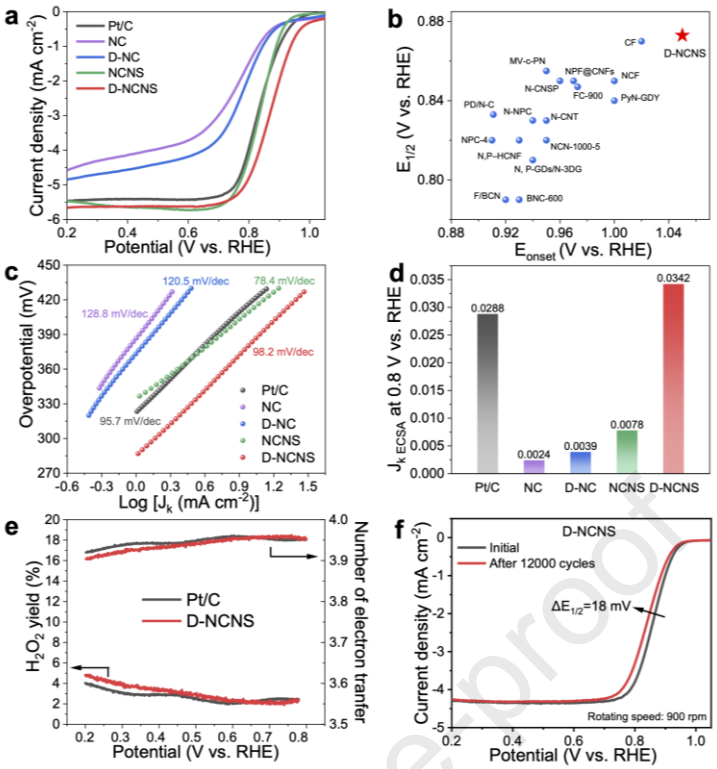

Figure 5. ORR performance. (a) ORR LSV curves for electrocatalysts, and (b) contrasting the E_{onset} and $E_{1/2}$ values for D-NCNS and the catalysts in the reported paper (the references are listed in Table S7). (c) Corresponding Tafel plots of ORR based on kinetic current (J_k). (d) Normalized by *ECSA* of specific J_k ($J_{k\ ECSA}$) at 0.8 V (vs. RHE) for electrocatalysts. (e) The number of electron transfer (n) and H_2O_2 yield percentage versus potential, and (f) the LSV curve of D-NCNS before and after accelerated degradation test of 12000 CV cycles.

3.4 Zinc–air battery performance

Considering the excellent ORR performance of D-NCNS, the ZABs assembled with D-NCNS air electrodes were studied. Commercial Pt/C was also tested as the catalyst of air cathode under the same conditions as the benchmark. The open-circuit voltage (OCV) of the ZAB using D-NCNS as the catalyst reaches 1.559 V (**Figure S25**), which is higher than ZAB with Pt/C air electrode (1.501 V). According to the discharge polarization curves (**Figure 6a**), the ZAB with D-NCNS exhibits a peak power density of 154.4 mW cm^{-2} at 384.3 mA cm^{-2}, better than that of ZAB with Pt/C (146.1 mW cm^{-2} at 221.4 mA cm^{-2}). The ZAB with D-NCNS shows a higher discharge voltage than that of ZAB with Pt/C at different discharge constant current densities from 1 mA cm^{-2} to 100 mA cm^{-2} (**Figure S26**), signifying that D-NCNS has a better rate performance than Pt/C in ZAB. The specific capacity is calculated based on the standardized mass of zinc consumed. As shown in **Figures 6b** and **S27**, the ZAB with D-NCNS presents a

high specific capacity (815.3 mAh g^{-1}) and energy density (1046.9 Wh kg^{-1}), which is higher than the ZAB with Pt/C (756.9 mAh g^{-1} and 955.9 Wh kg^{-1}). Long-term discharge stability of the Pt/C and D-NCNS in ZAB was evaluated by mechanically replacing Zn and 6 M KOH electrolytes. As shown in **Figure 6c–d**, the discharge voltage of ZAB using D-NCNS remains unchanged after more than 144 h (24 h × 6) of running time, whereas the ZAB with Pt/C failed after about 70 h. Interestingly, a light bulb or two small fans can be efficiently powered by a ZAB using D-NCNS as an air-cathode catalyst, as shown in **Figure 6e–f**. The results indicated that the superior ORR activity of D-NCNS electrocatalyst can potentially replace Pt/C and be applied in ZABs. The performance of D-NCNS and reported catalysts are listed in **Table S9** for comparison.

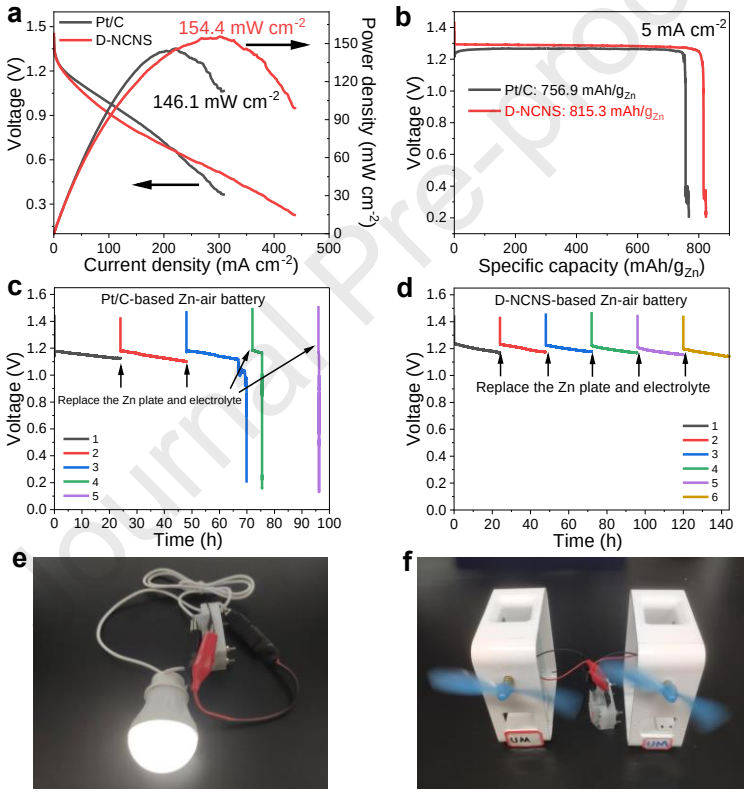

Figure 6. Zinc–air battery performance of commercial Pt/C and D-NCNS. (a) Discharge polarization curves and the corresponding power density plots. (b) Specific capacity of the Zn–air batteries using Pt/C and D-NCNS as the cathode catalysts. (c, d) Discharge durability of Zn–air battery based on commercial Pt/C (c) and D-NCNS (d). (e, f) Photograph of Zn–air batteries based on D-NCNS, which is lighting a bulb (e) and two small fans (f).

3.5 DFT calculations

To disclose the origin of the excellent ORR activity of D-NCNS, we conducted first-principle density functional theory (DFT) calculations based on the $4e^-$ ORR pathway in alkaline

media.[51,52] The characterization results in Section 3.2 suggest D-NCNS possesses abundant edges, carbon pentagons, and a high sp^3/sp^2 carbon ratio. Therefore, we investigated the ORR reaction on seven configurations derived from zigzag-edged graphene nanoribbon to reveal the role of nitrogen dopant, carbon pentagon, and sp^3 carbon (**Figures 7** and **S28**).[19,53]

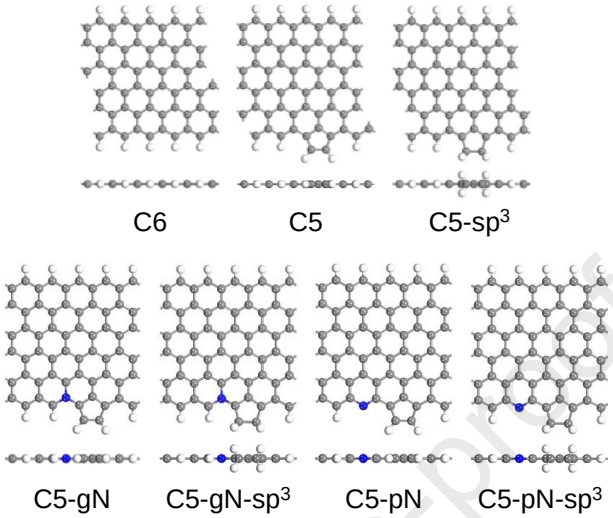

Figure 7. The proposed atomic structures for the DFT calculation study. The grey, blue and white balls represent C, N, and H atoms, respectively.

First, we calculated the Gibbs free energy diagrams of the configurations with different adsorbed oxygen intermediates. The schematic reaction pathway is shown in **Figure 8a**. C6 behaves with the largest overpotential among all configurations, revealing that pristine graphene is inactive in ORR (**Figure S29**). By introducing two sp^2 carbon atoms at the edge of C6, the overpotential of C5 lowers to 1.01 V, suggesting the positive role of carbon pentagon in ORR (**Figure 8b**).[17,53] If these two additional carbon atoms become sp^3 hybridization, the overpotential of C5-sp^3 significantly drops to 0.48 V. In addition, the rate-determining step (RDS) switches from O_2 activation for C5 to OH^- desorption for C5-sp^3. Interestingly, the introduction of pyridinic or graphitic nitrogen to C5 and C5-sp^3 leads to the raise of overpotential, implying the negative role of nitrogen doping in ORR (**Figure 9**).[18,19] This observation can be reflected by our experiments in Section 3.2, i. e. D-NCNS with lower nitrogen content (4.29 at%) outperforms NCNS with higher nitrogen content (5.93 at%). The low overpotential of C5-sp^3 indicates the combination of carbon pentagon and sp^3 hybridization carbon atoms can boost the ORR performance of NCMs.

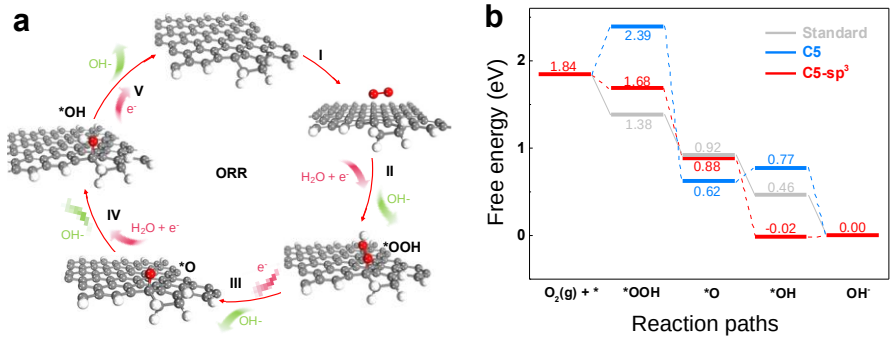

Figure 8. DFT calculation for ORR mechanism. (a) Scheme of ORR mechanism on the catalyst in alkaline electrolyte. The grey, red and white balls represent C, O, and H atoms, respectively. (b) Free energy diagram for ORR on various systems.

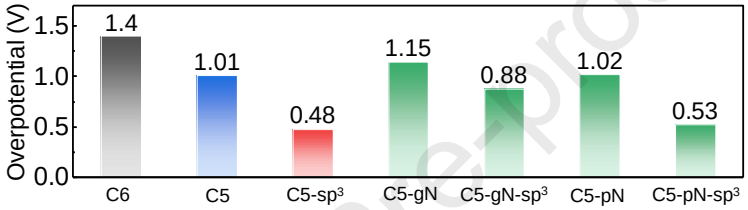

Figure 9. The calculated overpotentials of the studied catalytic systems.

To reveal the role of the sp^3/sp^2 carbon interface in carbon pentagon, we further studied the electronic structure of C5, C5-sp^3, and their related adsorption intermediates. Based on the projected density of state (PDOS) functions (**Figure 10a**), the spin-up orbital of C5 is partially occupied by the density of electron states in the vicinity of the Fermi level. In comparison, with the introduction of sp^3 carbon, the density of electron states near the Fermi level disappears, and the overall charge density becomes more diffuse. Meanwhile, a strong spin-down empty orbital appears above the Fermi level, which indicates the improved ability to gain electrons, hence the adsorption and activation of the O_2 molecule are strengthened. We further adopted crystal orbital Hamilton population (COHP) analysis to study the interaction between the catalytic active carbon atom and the terminal oxygen atom of *OOH intermediate (**Figure 10b** and **Figure S30**). The calculated integrated COHP (ICOHP) for C5-OOH and C5-sp^3-OOH is –4.05 eV and –4.45 eV, respectively. The higher absolute value of ICHOP for C5-sp^3-OOH indicates a stronger C–O interaction. This phenomenon can also be verified from the Bader charge analysis. When *OOH is adsorbed on C5, 0.46*e* of negative charge is transferred from the substrate to *OOH. In comparison, 0.53*e* is transferred when *OOH is adsorbed on C5-sp^3. The increased electron transfer further indicates that the adsorption capacity of C5-sp^3 for *OOH is enhanced. The above analysis shows that the introduction of sp^3 carbon in carbon

pentagon can strengthen the adsorption and activation of O_2 molecule on sp^2 carbon adjacent to sp^3 carbon, thus reducing the overpotential and improving the ORR activity.

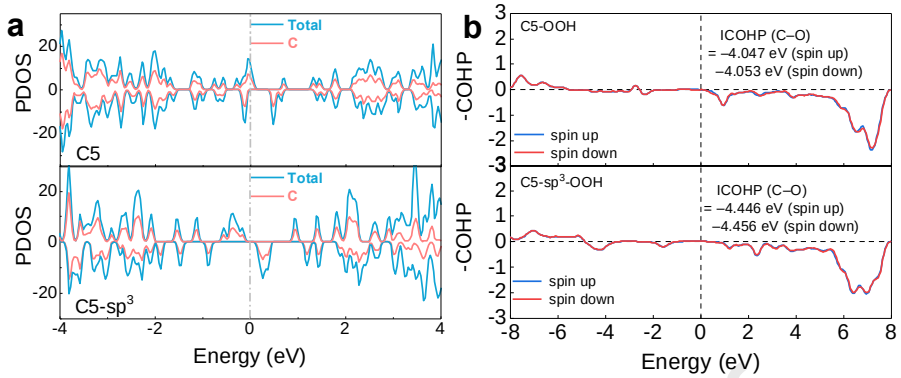

Figure 10. Electronic structure of C5, C5-sp^3, and *OOH adsorption intermediate. (a) The PDOS of C5 and C5-sp^3. (b) The COHP of C5 and C5-sp^3 after adsorbed *OOH.

3. Conclusion

In summary, we developed an H_3BO_3-assisted hydrothermal synthesis to generate ZIF-8 with linker vacancies and defective NCMs with subsequent pyrolysis. The as-synthesized D-NCNS electrocatalyst with high specific surface area, abundant edge sites, rich carbon pentagon, and high sp^3/sp^2 carbon ratio exhibits record-breaking ORR performance among the reported metal-free carbon-based materials. Theoretical calculation results disclose the synergistic effect of a topological defect (carbon pentagon) and hybridization states (sp^3/sp^2 carbon interface) to the superior ORR activity. Surprisingly, nitrogen doping does not benefit the ORR activity in our study. This work provides a new route to derive defective NCMs from defect-rich MOF precursors for energy conversion and storage applications.

CRediT authorship contribution statement

Haixing Gao: Conceptualization, Methodology, Investigation, Formal analysis, Investigation, Data curation, Drawing, Writing – original draft, Visualization. **Shuo Wang:** Methodology, Investigation, Formal analysis, Data curation, Drawing, Writing – original draft, Visualization. **Weng-Chon (Max) Cheong:** Conceptualization, Validation, Writing – review & editing, Visualization, Supervision, Funding acquisition. **Kaixi Wang:** Investigation. **Huifang Xu:** Investigation. **Aijian Huang**: Investigation, Formal analysis. **Junguo Ma**: Conceptualization, Writing – review & editing. **Jiazhan Li**: Funding acquisition, Formal analysis. **Weng-Fai (Andy) Ip:** Funding acquisition, Writing – review & editing. **Kwan San Hui:** Funding acquisition, Writing – review & editing. **Duc Anh Dinh:** Writing – review & editing. **Xi Fan:** Writing – review & editing. **Feng Bin:** Writing – review & editing. **Fuming Chen:** Writing – review & editing. **Kwun Nam Hui:** Resources, Writing – review & editing, Supervision, Project administration, Funding acquisition.

Declaration of Competing Interest

The authors declare that they have no known competing financial interests or personal relationships that could have appeared to influence the work reported in this paper.

Acknowledgments

This work was supported by the Science and Technology Development Fund (FDCT) of Macao S.A.R. (0041/2019/A1, 0046/2019/AFJ, 0021/2019/AIR, 0032/2021/ITP), the University of Macau (MYRG2018-00192-IAPME, MYRG2020-00187-IAPME), Beijing Municipal Natural Science Foundation (2214060), and the UEA funding. The DFT calculations were performed at the High-Performance Computing Cluster (HPCC) of the Information and Communication Technology Office (ICTO) at the University of Macau. Haixing Gao, Shuo Wang, and Weng-Chon (Max) Cheong contributed equally to this work.

Appendix A. Supplementary material

Supplementary data associated with this article can be found in the online version at doi:

References

[1] J. Zhang, J.J. Zhang, F. He, Y.J. Chen, J.W. Zhu, D.L. Wang, S.C. Mu, H.Y. Yang, 2021. Defect and doping co-engineered non-metal nanocarbon ORR electrocatalyst, Nano-Micro Lett. 13, 65. https://doi.org/10.1007/s40820-020-00579-y.

[2] C.G. Hu, R. Paul, Q.B. Dai, L.M. Dai, Carbon-based metal-free electrocatalysts: from oxygen reduction to multifunctional electrocatalysis, Chem. Soc. Rev. 50 (2021) 11785–11843. https://doi.org/10.1039/D1CS00219H.

[3] L.J. Zhang, T.T. Gu, K.L. Lu, L.J. Zhou, D.S. Li, R.H. Wang, 2021. Engineering synergistic edge-N dipole in metal-free carbon nanoflakes toward the intensified oxygen reduction electrocatalysis. Adv. Funct. Mater. 31, 2103187. https://doi.org/10.1002/adfm.202103187.

[4] X. Wang, Y. Jia, X. Mao, L.Z. Zhang, D.B. Liu, L. Song, X.C. Yan, J. Chen, D.J. Yang, J.Z. Zhou, K. Wang, A.J. Du, X.D. Yao, A directional synthesis for topological defect in carbon, Chem 6 (2020) 2009–2023. https://doi.org/10.1016/j.chempr.2020.05.010.

[5] J.W. Zhu, S.C. Mu, 2020. Defect engineering in the carbon-based electrocatalysts: insight into the intrinsic carbon defects, Adv. Funct. Mater. 30, 2001097. https://doi.org/10.1002/adfm.202001097.

[6] Q.F. Zhai, Y. Pan, L.M. Dai, Carbon-based metal-free electrocatalysts: past, present, and future, Acc. Mater. Res. 2 (2021) 1239–1250. https://doi.org/10.1021/accountsmr.1c00190.

[7] Y.X. Lu, L. Zhou, S.Y. Wang, Y.Q. Zou, Defect engineering of electrocatalysts for organic synthesis, Nano Res. (2022) https://doi.org/10.1007/s12274-022-4858-5.

[8] B.L. Yang, B.J. Li, Z.H. Xiang, Advanced MOF-based electrode materials for supercapacitors and electrocatalytic oxygen reduction, Nano Res. (2022) https://doi.org/10.1007/s12274-022-4682-y.

[9] C.X. Zhao, J.N. Liu, J. Wang, D. Ren, B.Q. Li, Q. Zhang, Recent advances of noble-metal-free bifunctional oxygen reduction and evolution electrocatalysts, Chem. Soc. Rev. 50 (2021) 7745–7778. https://doi.org/10.1039/D1CS00135C.

[10] Y.X. Wang, N.N. Xu, R.N. He, L.W. Peng, D.Q. Cai, J.L. Qiao, 2021. Large-scale defect-engineering tailored tri-doped graphene as a metal-free bifunctional catalyst for superior electrocatalytic oxygen reaction in rechargeable Zn-air battery. Appl. Catal. B-Environ. 285, 119811. https://doi.org/10.1016/j.apcatb.2020.119811.

[11] B. Wang, B.W. Liu, L.M. Dai, 2021. Non-N-doped carbons as metal-free electrocatalysts. Adv. Sustainable Syst. 5, 2000134. https://doi.org/10.1002/adsu.202000134.

[12] J. Ortiz-Medina, Z. P. Wang, R. Cruz-Silva, A. Morelos-Gomez, F. Wang, X.D. Yao, M. Terrones, M. Endo, 2019. Defect engineering and surface functionalization of nanocarbons for metal-free catalysis. Adv. Mater. 31, 1805717. https://doi.org/10.1002/adma.201805717.

[13] H.Y. Zhao, C.H. Sun, Z. Jin, D.W. Wang, X.C. Yan, Z.G. Chen, G.S. Zhu, X.D. Yao, Carbon for the oxygen reduction reaction: a defect mechanism, J. Mater. Chem. A 3 (2015) 11736–11739. https://doi.org/10.1039/C5TA02229K.

[14] A.L. Shen, Y.Q. Zou, Q. Wang, R.A.W. Dryfe, X.B. Huang, S. Dou, L.M. Dai, S.Y. Wang, Oxygen reduction reaction in a droplet on graphite: direct evidence that the edge is more active than the basal plane, Angew. Chem. Int. Ed. 53 (2014) 10804–10808. https://doi.org/10.1002/anie.201406695.

[15] C. Tang, H.F. Wang, X. Chen, B.Q. Li, T.Z. Hou, B.S. Zhang, Q. Zhang, M.M. Titirici, W. Fei, Topological defects in metal-free nanocarbon for oxygen electrocatalysis, Adv. Mater. 28 (2016) 6845–6851. https://doi.org/10.1002/adma.201601406.

[16] Y. Jia, L.Z. Zhang, A.J. Du, G.P. Gao, J. Chen, X.C. Yan, C.L. Brown, X.D. Yao, Defect graphene as a trifunctional catalyst for electrochemical reactions, Adv. Mater. 28 (2016) 9532–9538. https://doi.org/10.1002/adma.201602912.

[17] J.W. Zhu, Y.P. Huang, W.C. Mei, C.Y. Zhao, C.T. Zhang, J. Zhang, I.S. Amiinu, S.C. Mu, Effects of intrinsic pentagon defects on electrochemical reactivity of carbon nanomaterials, Angew. Chem. Int. Ed. 58 (2019) 3859–3864. https://doi.org/10.1002/anie.201813805.

[18] J. Gao, Y. Wang, H.H. Wu, X. Liu, L.L. Wang, Q.L. Yu, A.W. Li, H. Wang, C.Q. Song, Z.R. Gao, M. Peng, M.T. Zhang, N. Ma, J.O. Wang, W. Zhou, G.X. Wang, Z. Yin, D. Ma, Construction of a sp^3/sp^2 carbon interface in 3D N-doped nanocarbons for the oxygen reduction reaction, Angew. Chem. Int. Ed. 58 (2019) 15089–15097. https://doi.org/10.1002/anie.201907915.

[19] Y.J. Cao, Z. Liu, Y.T. Tang, C.J. Huang, Z.L. Wang, F. Liu, Y.W. Wei, B. Shan, R. Chen et al. Vaporized-salt-induced sp^3-hybridized defects on nitrogen-doped carbon surface towards oxygen reduction reaction, Carbon 180 (2021) 1–9. https://doi.org/10.1016/j.carbon.2021.04.059.

[20] L.Z. Zhuang, Y. Jia, H.L. Liu, X. Wang, R.K. Hocking, H.W. Liu, J. Chen, L. Ge, L.Z. Zhang, M.R. Li, C.L. Dong, Y.C. Huang, S.H. Shen, D.J. Yang, Z.H. Zhu, X.D. Yao, 2019. Defect-induced Pt-Co-Se coordinated sites with highly asymmetrical electronic distribution for boosting oxygen-involving electrocatalysis Adv. Mater. 31, e1805581. https://doi.org/10.1002/adma.201805581.

[21] S. Grimme, Semiempirical GGA-type density functional constructed with a long-range dispersion correction, J. Comput. Chem. 27 (2006) 1787–1799. https://doi.org/10.1002/jcc.20495.

[22] G. Kresse, J. Furthmüller, Efficient iterative schemes for ab initio total-energy calculations using a plane-wave basis set, Phys. Rev. B 54 (1996) 11169–11186. https://doi.org/10.1103/PhysRevB.54.11169.

[23] P.E. Blöchl, Projector augmented-wave method, Phys. Rev. B 50 (1994) 17953–17979. https://doi.org/10.1103/PhysRevB.50.17953.

[24] J.P. Perdew, Y. Wang, Pair-distribution function and its coupling-constant average for the spin-polarized electron gas, Phys. Rev. B 46 (1992) 12947–12954. https://doi.org/10.1103/PhysRevB.46.12947.

[25] H.J. Monkhorst, J.D. Pack, Special points for Brillouin-zone integrations, Phys. Rev. B 13 (1976) 5188–5192. https://doi.org/10.1103/PhysRevB.13.5188.

[26] S. Grimme, S. Ehrlich, L. Goerigk, Effect of the damping function in dispersion corrected density functional theory, J. Comput. Chem. 32 (2011) 1456–1465. https://doi.org/10.1002/jcc.21759.

[27] S. Grimme, J. Antony, S. Ehrlich, H. Krieg, 2010. A consistent and accurate ab initio parametrization of density functional dispersion correction (DFT-D) for the 94 elements H-Pu. J. Chem. Phys. 132, 154104. https://doi.org/10.1063/1.3382344.

[28] F. Yang, W.H. Hu, C.Q. Yang, M. Patrick, A.L. Cooksy, J. Zhang, J.A. Aguiar, C.C. Fang, Y.H. Zhou, Y.S. Meng, J.E. Huang, J. Gu, Tuning internal strain in metal–organic frameworks via vapor phase infiltration for CO_2 reduction, Angew. Chem. Int. Ed. 59 (2020) 4572–4580. https://doi.org/10.1002/anie.202000022.

[29] Y. Arafat, M.R. Azhar, Y.J. Zhong, H.R. Abid, M.O. Tadé, Z.P. Shao, 2021. Advances in zeolite imidazolate frameworks (ZIFs) derived bifunctional oxygen electrocatalysts and their application in zinc-air batteries. Adv. Energy Mater. 11, 2100514. https://doi.org/10.1002/aenm.202100514.

[30] C.Y. Zhang, C. Han, D.S. Sholl, J.R. Schmidt, Computational characterization of defects in metal-organic frameworks: spontaneous and water-induced point defects in ZIF-8, J. Phys. Chem. Lett. 7 (2016) 459–464. https://doi.org/10.1021/acs.jpclett.5b02683.

[31] N. Diez, A.B. Fuertes, M. Sevilla, Molten salt strategies towards carbon materials for energy storage and conversion, Energy Storage Mater. 38 (2021) 50–69. https://doi.org/10.1016/j.ensm.2021.02.048.

[32] X.T. Cao, R.L. Song, X.S. Zhou, X. Wang, X. Dong, N.Y. Yuan, J.N. Ding, 3D TM-N-C electrocatalysts with dense active sites for the membraneless direct methanol fuel cell and Zn-air batteries, Langmuir 38 (2022) 4948–4957. https://doi.org/10.1021/acs.langmuir.2c00347.

[33] L.B. Zong, W.C. Wu, S.L. Liu, H.J. Yin, Y.N. Chen, C. Liu, K.C. Fan, X.X. Zhao, X. Chen, F.M. Wang, Y. Yang, L. Wang, S.H. Fang, Metal-free, active nitrogen-enriched, efficient bifunctional oxygen electrocatalyst for ultrastable zinc-air batteries, Energy Storage Mater. 27 (2020) 514–521. https://doi.org/10.1016/j.ensm.2019.12.013.

[34] Y. Zhu, Z.Y. Zhang, W.Q. Li, Z. Lei, N.C. Cheng, Y.Y. Tan, S.C. Mu, S.L. Sun, Highly exposed active sites of defect-enriched derived MOFs for enhanced oxygen reduction reaction, ACS Sustainable Chem. Eng. 7 (2019) 17855–17862. https://doi.org/10.1021/acssuschemeng.9b04380.

[35] J. Yang, F. Xiang, H. Guo, L.P. Wang, X.B. Niu, Honeycomb-like porous carbon with N and S dual-doping as metal-free catalyst for the oxygen reduction reaction, Carbon 156 (2020) 514–522. https://doi.org/10.1016/j.carbon.2019.09.087.

[36] G. Wu, C.M. Johnston, N.H. Mack, K. Artyushkova, M. Ferrandon, M. Nelson, J.S. Lezama-Pacheco, S.D. Conradson, K.L. More, D.J. Myers, P. Zelenay, Synthesis–structure–performance correlation for polyaniline–Me–C non-precious metal cathode catalysts for oxygen reduction in fuel cells, J. Mater. Chem. 21 (2011) 11392–11405. https://doi.org/10.1039/C0JM03613G.

[37] S. Mukherjee, D.A. Cullen, S. Karakalos, K.X. Liu, H. Zhang, S. Zhao, H. Xu, K.L. More, G.F. Wang, G. Wu, Metal-organic framework-derived nitrogen-doped highly disordered carbon for electrochemical ammonia synthesis using N_2 and H_2O in alkaline electrolytes, Nano Energy 48 (2018) 217–226. https://doi.org/10.1016/j.nanoen.2018.03.059.

[38] Sadezky, H. Muckenhuber, H. Grothe, R. Niessner, U. Pöschl, Raman microspectroscopy of soot and related carbonaceous materials: spectral analysis and structural information, Carbon 43 (2005) 1731–1742. https://doi.org/10.1016/j.carbon.2005.02.018.

[39] Q. Lv, N. Wang, W.Y. Si, Z.F. Hou, X.D. Li, X. Wang, F.H. Zhao, Z. Yang, Y.L. Zhang, C.S. Huang, 2020. Pyridinic nitrogen exclusively doped carbon materials as efficient oxygen reduction electrocatalysts for Zn-air batteries. Appl. Catal. B-Environ. 261, 118234. https://doi.org/10.1016/j.apcatb.2019.118234.

[40] G. Wu, N.H. Mack, W. Gao, S.G. Ma, R.Q. Zhong, J.T. Han, J.K. Baldwin, P. Zelenay, Nitrogen-doped graphene-rich catalysts derived from heteroatom polymers for oxygen reduction in nonaqueous lithium-O_2 battery cathodes, ACS Nano 6 (2012) 9764–9776. https://doi.org/10.1021/nn303275d.

[41] Y.Q. Wang, L. Tao, Z.H. Xiao, R. Chen, Z.Q. Jiang, S.Y. Wang, 2018. 3D carbon electrocatalysts in situ constructed by defect-rich nanosheets and polyhedrons from NaCl-sealed zeolitic imidazolate frameworks. Adv. Funct. Mater. 28, 1705356. https://doi.org/10.1002/adfm.201705356.

[42] M.P. Jian, B. Liu, R.P. Liu, J.H. Qu, H.T. Wang, X.W. Zhang, Water-based synthesis of zeolitic imidazolate framework-8 with high morphology level at room temperature, RSC Adv. 5 (2015) 48433–48441. https://doi.org/10.1039/C5RA04033G.

[43] K. Kida, M. Okita, K. Fujita, S. Tanaka, Y. Miyake, Formation of high crystalline ZIF-8 in an aqueous solution, CrystEngComm, 15 (2013) 1794–1801. https://doi.org/10.1039/C2CE26847G.

[44] J. Troyano, A. Carne-Sanchez, C. Avci, I. Imaz, D. Maspoch, Colloidal metal-organic framework particles: the pioneering case of ZIF-8, Chem. Soc. Rev. 48 (2019) 5534–5546. https://doi.org/10.1039/C9CS00472F.

[45] Y. Chang, J.X. Chen, J.C. Jia, X. Hu, H.J. Yang, M.L. Jia, Z.H. Wen, 2021. The fluorine-doped and defects engineered carbon nanosheets as advanced electrocatalysts for oxygen

electroreduction. Appl. Catal. B-Environ. 284, 119721. https://doi.org/10.1016/j.apcatb.2020.119721.

[46] R.P. Zhao, Q.H. Li, Z.J. Chen, V. Jose, X. Jiang, G.T. Fu, J.M. Lee, S.M. Huang, B, N-doped ultrathin carbon nanosheet superstructure for high-performance oxygen reduction reaction in rechargeable zinc-air battery, Carbon 164 (2020) 398–406. https://doi.org/10.1016/j.carbon.2020.04.019.

[47] K.L. Hu, T.T. Yu, Y.Y. Zhang, X.R. Lin, Y.L. Zhao, G.Q. Xie, X.J. Liu, X. Lin, J.I. Fujita, H.J. Qiu, Y. Ito, 2021. Inhibiting surface diffusion to synthesize 3D bicontinuous nanoporous N-doped carbon for boosting oxygen reduction reaction in flexible all-solid-state Al-air batteries. Adv. Funct. Mater. 31, 2103632. https://doi.org/10.1002/adfm.202103632.

[48] M.A. Ahsan, T.W. He, K. Eid, A.M. Abdullah, M.L. Curry, A.J. Du, A.R.P. Santiago, L. Echegoyen, J.C. Noveron, Tuning the intermolecular electron transfer of low-dimensional and metal-free BCN/C_{60} electrocatalysts via interfacial defects for efficient hydrogen and oxygen electrochemistry, J. Am. Chem. Soc. 143 (2021) 1203–1215. https://doi.org/10.1021/jacs.0c12386.

[49] X. Wang, Y. Jia, X. Mao, D.B. Liu, W.X. He, J.G. Li, X. C. Yan, J. Chen, L. Song, A.J. Du, X.D. Yao, 2020. Edge-rich Fe-N_4 active sites in defective carbon for oxygen reduction catalysis. Adv. Mater. 32, e2000966. https://doi.org/10.1002/adma.202000966.

[50] F. Li, Y.F. Bu, G.F. Han, H.J. Noh, S.J. Kim, I. Ahmad, Y.L. Lu, P. Zhang, H.Y. Jeong, Z.P. Fu, Q. Zhong, J.B. Baek, 2019. Identifying the structure of Zn-N_2 active sites and structural activation. Nat. Commun. 10, 2623. https://doi.org/10.1038/s41467-019-10622-1.

[51] L.C. Seitz, T.J. Hersbach, D. Nordlund, T.F. Jaramillo, Enhancement effect of noble metals on manganese oxide for the oxygen evolution reaction, J. Phys. Chem. Lett. 6 (2015) 4178–4183. https://doi.org/10.1021/acs.jpclett.5b01928.

[52] H. Dau, C. Limberg, T. Reier, M. Risch, S. Roggan, P. Strasser, The mechanism of water oxidation: from electrolysis via homogeneous to biological catalysis, ChemCatChem, 2 (2010) 724–761. https://doi.org/10.1002/cctc.201000126.

[53] S. Liu, Y.C. Zhang, B.H. Ge, F.C. Zheng, N. Zhang, M. Zuo, Y. Yang, Q.W. Chen, 2021. Constructing graphitic-nitrogen-bonded pentagons in interlayer-expanded graphene matrix toward carbon-based electrocatalysts for acidic oxygen reduction reaction. Adv. Mater. 33, e2103133. https://doi.org/10.1002/adma.202103133.

Highlights

- Hydrothemal synthesis of ZIF-8 with linker vacancies by addition of boric acid
- Rich edge sites, carbon pentagon and sp^3 hybrization in derived metal-free carbon
- Superior ORR and zinc–air battery performance among reported metal-free materials
- Synergistic effect of topological defect and hybrization state

Declaration of interests

☒ The authors declare that they have no known competing financial interests or personal relationships that could have appeared to influence the work reported in this paper.

☐ The authors declare the following financial interests/personal relationships which may be considered as potential competing interests: